Magic continuum in a twisted bilayer square lattice with staggered flux

Zhu-Xi Luo (罗竹悉)⁰, Cenke Xu, and Chao-Ming Jian³ ¹Kavli Institute for Theoretical Physics, University of California, Santa Barbara, California 93106, USA ²Department of Physics, University of California, Santa Barbara, California 93106, USA ³Department of Physics, Cornell University, Ithaca, New York 14853, USA

(Received 13 April 2021; revised 5 July 2021; accepted 6 July 2021; published 19 July 2021)

We derive the general continuum model for a bilayer system of staggered-flux square lattices, with arbitrary elastic deformation in each layer. Applying this general continuum model to the case where the two layers are rigidly rotated relative to each other by a small angle, we obtain the band structure of the twisted bilayer staggered-flux square lattice. We show that this band structure exhibits a magic continuum in the sense that an exponential reduction of the Dirac velocity and bandwidths occurs in a large parameter regime. We show that the continuum model of the twisted bilayer system effectively describes a massless Dirac fermion in a spatially modulating magnetic field, whose renormalized Dirac velocity can be exactly calculated. We further give an intuitive argument for the emergence of flattened bands near half filling in the magic continuum and provide an estimation of the large number of associated nearly zero-energy states. We also show that the entire band structure of the twisted bilayer system is free of band gaps due to symmetry constraints.

DOI: 10.1103/PhysRevB.104.035136

I. INTRODUCTION

The experimental observations of correlated insulating and superconducting behaviors in twisted bilayer graphene [1–9] have generated the era of twistronics [10]. Since then, moiré physics of various assembled atomically thin systems has been explored, including transition metal dichalgonide heterostructures [11-18], other graphene-based heterostructures such as twisted double bilayer graphene [19-22], ABC-stacked trilayer graphene/boron nitride [23-25], twisted monolayerbilayer graphene [26], and twisted trilayer graphene [27]. There have also been theoretical proposals of other exotic moiré systems, for example, bilayers of general Bravais lattices [28], van der Waals magnets [29], superconductors [30,31], gapped spin liquid [32], surface states of topological insulators [33,34], and cold atomic systems [35–38], to name a few.

The correlated behaviors in twisted bilayer graphene are known to be associated with the flattening of bands near the charge neutrality. Such band flattening was theoretically predicted [39-42] and experimentally observed [1,2,43]. In fact, the widths of the energy bands near the charge neutrality are highly sensitive to the twist angles in the twisted bilayer graphene system. The flat bands only occur inside very narrow windows around certain discrete values of magic angles [39]. However, it is experimentally challenging to precisely control the twist angles between the two graphene sheets. Different samples tend to settle into configurations with different twist angles or even spatially inhomogeneous twist angles. The high sensitivity of the electronic structure makes it difficult to interpret experimental measurements of correlated physics and understand their underlying mechanisms in such systems. It would then be much more ideal if the band flattening happens in a wide range of twist angles. An interesting example of such a scenario is given by twisted bilayer WSe₂, which is experimentally shown to exhibit band flattening and associated correlated physics over a continuum range of twist angles. This continuum range of twist angles is referred to as the magic continuum [18]. However, we note that gapless Dirac cones, a prominent feature of the electronic structure of twisted bilayer graphene, is not present in the twisted bilayer WSe₂ system. It is interesting to search for systems with both gapless Dirac cones near charge neutrality and a magic continuum of twist angles where band flattening occurs.

The gapless Dirac cones of twisted bilayer graphene are inherited from those of each individual graphene sheet. As a generalization, it is natural to consider twisted bilayer systems where Dirac cones are present in the electronic structure of each individual layer. In this paper, we will focus on a twisted bilayer system consisting of two layers of staggered-flux square lattice. A single-layer staggered-flux square lattice describes a tight-binding model with nearestneighbor hoppings on the square lattice subject to a staggered magnetic flux pattern. The band structure of this tight-binding model contains two gapless Dirac cones at half filling. This staggered-flux square-lattice model was initially proposed to capture the band structure of fractionalized particles in underdoped cuprates [44-48] (see Ref. [49] for a review). It has also been widely investigated as a prominent mean-field ansatz for an algebraic quantum spin liquid [50-54] that can be viewed as a parent state of many competing orders [54]. In the contexts of both cuprates and spin liquids, it is the fractionalized particles (i.e., spinons) that experience the staggered flux on the square lattice. In our paper, we will focus on the case where the staggered-flux square-lattice tight-binding model describes the hopping of electrons within each layer of our bilayer system. The examination of the moiré physics of a bilayer staggered-flux square lattice will also serve as a preceding step toward understanding the physics of a twisted bilayer of algebraic spin liquids.

In a seminal work [39], a continuum model was developed to describe the band structure of twisted bilayer graphene. This continuum model and its generalizations have been the foundation of theoretical studies of twisted bilayer graphene and other moiré systems. The method based on continuum models has proven to be advantageous for general moiré systems: It restores periodicity in a quasiperiodic system, reduces the number of dimensionless parameters, and is flexible to incorporate general smooth deformations. Following the method introduced in Ref. [39], continuum models of bilayer or multilayer moiré systems can be obtained by studying reasonable forms of interlayer tunnelings in momentum space. Recently, a real-space derivation of the continuum model for twisted bilayer graphene has been developed [55]. In this derivation, the original continuum model of twisted bilayer graphene was directly obtained from symmetry-based bootstrap analysis. More generally, as shown in Ref. [55], the same method enables the derivation of the continuum model of general bilayer graphene systems with arbitrary independent elastic deformation in each graphene layer. In this paper, we follow the real-space symmetry-based method to construct the continuum model for arbitrary elastically deformed bilayer of the staggered-flux square lattice.

A case of particular interest is the twisted bilayer staggered-flux square lattice system where the two layers of square lattices are rigidly rotated relative to each other by a small twist angle. We solve the corresponding continuum model for the band structure and find that a gapless Dirac cone exists near half filling with the Dirac velocity is substantially renormalized compared to that in a single-layer staggered-flux square lattice. In particular, it decreases exponentially as the interlayer tunneling increases and/or as the the twist angle decreases. Indicated by the drastic reduction of the Dirac velocity, the flattening of the bands near half filling occurs in a large regime of the tunneling parameter and twist angles, i.e., there is a magic continuum. This magic continuum can be understood as arising from Dirac fermions subject to a spatially periodically modulated effective magnetic field induced by the interlayer tunneling. Also, we show that the band structure of the twisted bilayer staggered-flux square lattice system is free of band gaps at any energy. The symmetries of system enforce all the bands to be connected to the neighboring ones. This infinite connectivity of all the bands in the twisted bilayer staggered-flux square lattice system is similar to the "perfect metal" discussed in graphene-based heterostructures [56,57].

The remainder of this paper is organized as follows. In Sec. II, we review the tight-binding model of a single-layer staggered-flux square lattice and its low-energy continuum model for the band structure. We further extend the continuum model to incorporate an arbitrary elastic deformation of the square lattice. In Sec. III, we consider a bilayer system with two elastically deformed staggered-flux square lattice layers. We present the symmetry-based bootstrap analysis of the general form of the Hamiltonian of the bilayer system in Sec. III A. In Secs. III B and III C, we apply the general

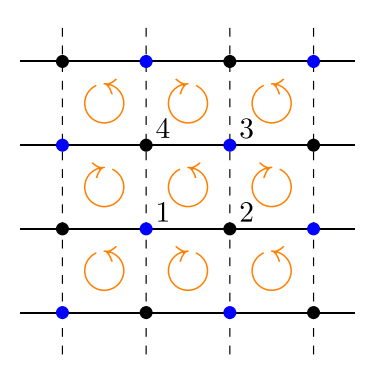


FIG. 1. The square lattice with staggered flux is shown. The blue/black dots correspond to the A/B sublattice, respectively. The hopping amplitudes from sublattices A to B through solid black links are given by $(it + \Delta)$, while those through the dashed links are given by $(it - \Delta)$. The neighboring plaquettes thus host staggered flux $\pm \Phi$. To obtain the spectrum, we consider a four-site unit cell with the four sites within a unit cell labeled as shown above.

Hamiltonian to the two special cases, respectively, (1) bilayer systems with two square-lattice layers rigidly shifted relative to each other and (2) twisted bilayer systems with two square-lattice layers rigidly rotated relative to each other by a small twist angle. We also present the numerical calculation of band structures of the twisted bilayer system. In Sec. IV, we perform a more detailed analytical study on the band structure of twisted bilayer system. In particular, we show analytically the drastic reduction of Dirac velocity as we increase the interlayer tunneling (or decrease the twist angle). We present an intuitive argument for the emergence of flattened bands and the large number of associated low-energy states in the same parameter regime. We also discuss a symmetry-based argument that enforces the infinite connectivity of the entire band structure. We then conclude with some extensions and outlook in Sec. V.

II. SINGLE-LAYER CONTINUUM MODEL

In this section, we first review the basics of the staggeredflux square-lattice tight-binding model, and then derive a continuum model that incorporates an arbitrary smooth lattice deformation.

A. Review of staggered-flux square-lattice model

The Hamiltonian of the staggered-flux square-lattice model describes spinful fermions hopping on the square lattice, divided into two sublattices *A* and *B*:

$$H = -\sum_{r \in A} \sum_{r' \in n.n.} [(it + (-1)^{r_y - r'_y} \Delta) f_{r\alpha}^{\dagger} f_{r'\alpha} + \text{H.c.}], \quad (1)$$

where $\sum_{r \in A}$ is a summation over the sites in the sublattice A and $\sum_{r' \in n.n.}$ sums over the B-sublattice sites r' that are the nearest neighbors of r. The subscript α is the spin index. The hopping amplitudes are shown in Fig. 1. This Hamiltonian describes fermions hopping in a background of staggered magnetic flux. The flux though each square plaquette is given

by $\pm \Phi = \pm 4 \arctan(t/\Delta)$. The signs of fluxes are opposite for neighboring plaquettes.

The naive translations by one site along the x and y directions do not leave the Hamiltonian in Eq. (1) invariant. Such translations, when combined with an extra particle-hole transformation, become the symmetries of the Hamiltonian. We denote these spatial translations followed by a particle-hole transformation as T_x and T_y . Similarly, the Hamiltonian has a mirror symmetry \mathcal{M}_x that maps the site at $\mathbf{r} = (r_x, r_y)$ to the site at $\mathcal{M}_x \mathbf{r} \equiv (-r_x, r_y)$ and, at the same time, maps particles to holes. Moreover, the Hamiltonian has a time-reversal symmetry \mathcal{T} and a plaquette-centered fourfold spatial rotation symmetry $R_{\frac{\pi}{2}}$ that transform the sites following $\mathbf{r} \to R_{\frac{\pi}{2}} \mathbf{r} \equiv (-r_y + 1, r_x)$. The actions of these symmetries on the lattice fermions are given by

$$T_{x}: f_{r,\alpha} \to \epsilon_{r}(i\sigma^{2})_{\alpha\beta}f_{r+\hat{x},\beta}^{\dagger},$$

$$T_{y}: f_{r,\alpha} \to \epsilon_{r}(i\sigma^{2})_{\alpha\beta}f_{r+\hat{y},\beta}^{\dagger},$$

$$\mathcal{M}_{x}: f_{r,\alpha} \to f_{\mathcal{M}_{x}r,\alpha},$$

$$R_{\frac{\pi}{2}}: f_{r,\alpha} \to \epsilon_{r}f_{R_{\frac{\pi}{2}}r,\alpha},$$

$$\mathcal{T}: f_{r,\alpha} \to \epsilon_{r}f_{r,\alpha}^{\dagger},$$

$$(2)$$

where $\sigma = (\sigma^1, \sigma^2, \sigma^3)$ acts in the SU(2)-spin space and ϵ_r takes value 1 for sublattice A and -1 for sublattice B. The transformation laws for f^{\dagger} 's can be obtained by taking the Hermitian conjugate on both sides of the transformation laws above in Eqs. (2). In the context of algebraic spin liquids, these transformations were initially introduced as the projective symmetry group acting on the fermionic spinons that couples to dynamical gauge fields [51]. In this paper, we view these transformations as the actual symmetry action on gauge-neutral fermions hopping on the staggered-flux square lattice.

To obtain the band structure of the Hamiltonian Eq. (1), we take a four-site unit cell on the square lattice as shown in Fig. 1, following the convention in Ref. [54]. Each unit cell is assigned a coordinate $\mathbf{R} = (R_x, R_y)$ with both R_x and R_y even integers. The four sites labeled by the i = 1, 2, 3, 4 are located at $\mathbf{r}(\mathbf{R}, i) = \mathbf{R} + \mathbf{v}_i$, where

$$\mathbf{v}_{i} = \begin{cases} 0, & i = 1\\ \hat{\mathbf{x}}, & i = 2\\ \hat{\mathbf{x}} + \hat{\mathbf{y}}, & i = 3\\ \hat{\mathbf{y}}, & i = 4. \end{cases}$$
 (3)

Sublattice A corresponds to i = 1, 3 while sublattice B corresponds to i = 2, 4. The fermion operator at $r(\mathbf{R}, i)$ will be denoted as $f_{\mathbf{R}i\alpha}$.

The energy spectrum of the model Eq. (1) is given by

$$\varepsilon(\mathbf{k}) = \pm 2 \left[\pm 2(\Delta^2 - t^2) \cos k_x \cos k_y + \frac{1}{2}(\Delta^2 + t^2)(2 + \cos 2k_x + \cos 2k_y) \right]^{1/2}, \quad (4)$$

where the two \pm signs are independent of each other. The four combinations of \pm signs correspond to four different bands. In the reduced Brillouin zone k_x , $k_y \in [0, \pi)$, there is a gapless point at $K = (\pi/2, \pi/2)$ at half filling, as shown in Fig. 2. In this model, half filling occurs at zero energy due to the

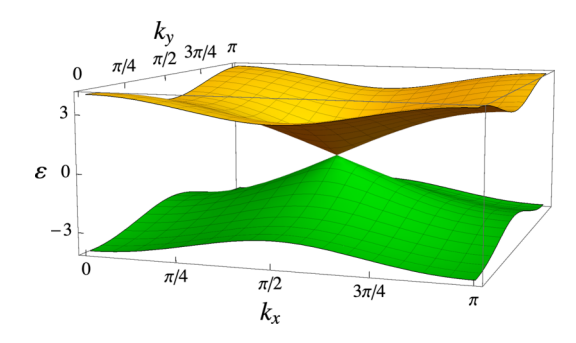


FIG. 2. Spectrum of the monolayer staggered-flux square lattice with $t = \Delta = 1$. There are two degenerate Dirac cones for each spin located at $K = (\pi/2, \pi/2)$ in the reduced Brillouin zone.

symmetry \mathcal{T} . One observes that the position of the gapless point is independent of t/Δ . This gapless point can be captured by two gapless Dirac cones in a continuum description. The ratio t/Δ controls the Dirac velocity anisotropy of these Dirac cones. In this paper, we will focus on the isotropic limit where $t/\Delta=1$, but the main features of our final results remain robust when anisotropy is present [58].

To obtain the continuum model for the gapless Dirac cones at half filling, we expand the Hamiltonian around the K point and introduce the Dirac fermions basis $\psi^I_{a\alpha}(R)$ in the following way:

$$\begin{pmatrix} f_{R1\alpha} \\ f_{R2\alpha} \\ f_{R3\alpha} \\ f_{R4\alpha} \end{pmatrix} \sim e^{-i\mathbf{K}\cdot\mathbf{R}} \begin{pmatrix} 1 & 0 & 0 & e^{-3i\pi/4} \\ 0 & i & e^{-3i\pi/4} & 0 \\ 1 & 0 & 0 & e^{i\pi/4} \\ 0 & -i & e^{-3i\pi/4} & 0 \end{pmatrix} \begin{pmatrix} \psi_{1\alpha}^1 \\ \psi_{2\alpha}^1 \\ \psi_{2\alpha}^2 \\ \psi_{2\alpha}^2 \end{pmatrix} (\mathbf{R}).$$
(5)

Here the superscript I=1,2 of $\psi_{a\alpha}^I$ labels the two components of a Dirac spinor, and the subscripts a=1,2 and $\alpha=1,2$ label the valley and spin degrees of freedom, respectively. Denoting the deviation of momentum k from the K point as q, i.e., $q \equiv k - K$, and further switching to the 45° -rotated coordinates, $q_1 = \frac{1}{\sqrt{2}}(q_x + q_y)$, $q_2 = \frac{1}{\sqrt{2}}(-q_x + q_y)$, the continuum Hamiltonian becomes

$$H = \int \frac{d^2 \mathbf{q}}{(2\pi)^2} \, \psi^{\dagger}(\mathbf{q}) (q_1 \tau^1 + q_2 \tau^2) \psi(\mathbf{q}), \tag{6}$$

where we have set the Dirac velocity to be 1 and $\tau = (\tau^1, \tau^2, \tau^3)$ are the Pauli matrices acting in the Dirac spinor space, the space indexed by the superscript I=1,2 of the Dirac fermions $\psi^I_{a\alpha}$. We also introduce the Pauli matrices $\mu=(\mu^1,\mu^2,\mu^3)$ that act on the twofold valley space. The Pauli matrices μ generate the SU(2)_{valley} rotation of the Dirac fermions ψ . The continuum Hamiltonian manifestly has the SU(4) \supset SU(2)_{spin} \times SU(2)_{valley} symmetry generated by $\{\sigma^i,\mu^i,\sigma^i\mu^j\}$. Here, remember that σ generates the SU(2)_{spin} rotation of the Dirac fermions.

In the following, we will suppress the Dirac spinor index I, valley index a, and spin index α and write ψ as the shorthand notation for the eight-component Dirac spinor $\psi^I_{\alpha\alpha}$. The

symmetries listed in Eqs. (2) then act on the Dirac fermions as

$$T_{x}: \quad \psi(\mathbf{R}) \to \sigma^{2} \tau^{1} \psi^{*}(\mathbf{R}),$$

$$T_{y}: \quad \psi(\mathbf{R}) \to -\sigma^{2} \mu^{3} \tau^{1} \psi^{*}(\mathbf{R}),$$

$$\mathcal{M}_{x}: \quad \psi(\mathbf{R}) \to W_{1} \psi(\mathcal{M}_{x} \mathbf{R}),$$

$$R_{\frac{\pi}{2}}: \quad \psi(\mathbf{R}) \to W_{2} \psi(R_{\frac{\pi}{2}} \mathbf{R}),$$

$$\mathcal{T}: \quad \psi(\mathbf{R}) \to -\mu^{3} \tau^{3} \psi^{*}(\mathbf{R}),$$

$$(7)$$

where $W_1=(-i\mu^2)\exp[\frac{i\pi}{2}(\frac{\tau^1+\tau^2}{\sqrt{2}})]$ and $W_2=e^{3i\pi/4}\exp[\frac{i\pi}{2}(\frac{\mu^1+\mu^2}{\sqrt{2}})]\exp(\frac{i\pi}{4}\tau^3)$. The transformation laws for ψ^{\dagger} 's can be obtained by taking the Hermitian conjugate on both sides of the transformation laws in Eqs. (7).

B. Elastic deformation

Now we move on to the elastically deformed version of the staggered-flux square lattice. The derivation of the continuum Hamiltonian closely follows the formalism developed in Ref. [55] in the context of twisted bilayer graphene.

In the following, we will make use of the Eulerian coordinates

$$x = R + u(x), \tag{8}$$

where x is the spatial coordinate of sites in the deformed lattice, \mathbf{R} is the coordinate of the same lattice site prior to the deformation, and u describes the deformation. We will assume that $\partial u \ll 1$, such that the elasticity theory applies. Notice that u(x) and R are both treated as functions of the Eulerian coordinate x. An alternative choice of coordinate system is the Lagrangian coordinate where x and u are both treated as functions of \mathbf{R} , the spatial coordinate of the predeformed lattice site. We choose to use the Eulerian coordinate x over the Lagrangian coordinate R for the purpose of our later discussion on the bilayer system with the two layers independently deformed. Two points in the two layers that share the same Lagrangian coordinate R can be far part due to the independent deformation in each layer. Therefore, the spatial locality in the deformed bilayer system is not manifest in the Lagrangian coordinate R. In contrast, being the realspace coordinates of lattice sites after the deformation, the Eulerian coordinate x avoids this problem.

The fermion modes $f_{Ri\alpha}$, its associated Hamiltonian, and symmetry transformations introduced in Sec. II are all formulated in the Lagrangian coordinate R. In the following, we will suppress the subscripts i and α in the fermion operator f_R for simplicity. In the presence of elastic deformation, we should view Eq. (8) as a coordinate transformation that induces a new set of fermion operators $f_x = |\det(\partial R_\mu)/(\partial x_\nu)|^{1/2} f_{R(x)} \sim (1 - \nabla \cdot \boldsymbol{u})^{1/2} e^{-iK \cdot (x - \boldsymbol{u}(x))} U \psi(R(x))$, where the Jacobian $|\det(\partial R_\mu)/(\partial x_\nu)|^{1/2}$ is required to ensure the correct fermionic anticommutation relations and U is the 4×4 matrix introduced in Eq. (5) which only acts on the valley and Dirac spinor indices (but not the spin index) of ψ . We can define the Dirac fermion operator $\psi(x)$ in the Eulerian coordinate via $f_x \sim e^{-iK \cdot x} U \psi(x)$, leading to the relation

$$\psi(\mathbf{R}) = (1 - \nabla \cdot \mathbf{u})^{-1/2} e^{-i\mathbf{K} \cdot \mathbf{u}} \psi(\mathbf{x}). \tag{9}$$

Note that the Dirac fermion operator $\psi(x)$ in the Eulerian coordinate shares the same Dirac spinor, valley, and spin indices as its Lagrangian-coordinate counterpart $\psi(R)$. Furthermore, under the coordinate change Eq. (8), the integration measure and the derivative change as $d^2R \approx d^2x(1 - \nabla \cdot u)$ and $\partial/\partial R_i \approx \partial/\partial x_i + (\partial u_j/\partial x_i)(\partial/\partial x_j)$ up to the first order in the derivative of u. Now, we can rewrite the continuum Hamiltonian Eq. (6) currently defined on a deformed lattice as a continuum Hamiltonian in the real space (parameterized by the Eulerian coordinate x):

$$H_0 = -i \int d^2 \mathbf{x} \ \psi^{\dagger}(\mathbf{x}) [\tau^i \partial_i + \tau^j (\partial_j u^i) \partial_i - i \tau^i K_j \partial_i u^j] \psi(\mathbf{x}).$$
(10)

Here, we have only kept the terms up to the first-order derivative of u. In this equation, $\partial_i = \partial/\partial x_i$ with i = 1, 2 are the derivatives with respect to the 45°-rotated version of the coordinate x. We remark that the second term $\psi^{\dagger} \tau^j (\partial_j u^i) \partial_i \psi$ captures the rotation of the Dirac cone under the deformation while the third term $K_i \nabla u_i$ in this equation captures the shift of the Dirac point in the momentum space.

Each symmetry listed in Eqs. (7) leads to a symmetry in the continuum theory Eq. (10) of the deformed lattice. Due to the change of coordinates Eq. (8), the form of symmetry actions on the Dirac fermion $\psi(x)$ will be different from Eqs. (7). Moreover, for the space-group symmetries, including the mirror symmetry \mathcal{M}_x and the fourfold rotation symmetry $R_{\frac{\pi}{2}}$, the continuum theory should only be invariant under the simultaneous transformation of both the Dirac fermion $\psi(x)$ and the deformation field u(x). Even though the symmetries $T_{x,y}$ are also space-group symmetry at the lattice scale, they should be viewed as internal symmetries that only act on the Dirac spinor and the valley indices in the continuum theory. Therefore, $T_{x,y}$ should not involve any nontrivial action on the deformation field u(x). The time-reversal symmetry \mathcal{T} should also keep the deformation field u(x) invariant.

Now we derive the form of symmetry actions for the continuum model Eq. (10). Take T_x as an example: If we were to take the same transformation law as that in Eqs. (7), then among the three terms in the square bracket of Eq. (10), the first two terms are invariant, while the third term changes by a sign. To compensate for this sign change, we introduce an additional phase to the transformation:

$$T_x: \quad \psi(\mathbf{x}) \to e^{2i\mathbf{K}\cdot\mathbf{u}(\mathbf{x})} \sigma^2 \tau^1 \psi^*(\mathbf{x}).$$
 (11)

This extra phase will give an additional contribution to the first term in Eq. (10), thereby keeping the full Hamiltonian invariant [without additional transformation on u(x)]. Physically, this extra phase factor reflects the shift of the Dirac cones in the momentum space introduced by the deformation u(x). In the presence of deformation u(x), all symmetry transformations of the fermion operators are summarized as follows:

$$T_{x}: \quad \psi(\mathbf{x}) \to e^{2i\mathbf{K}\cdot\mathbf{u}(\mathbf{x})}\sigma^{2}\tau^{1}\psi^{*}(\mathbf{x}),$$

$$T_{y}: \quad \psi(\mathbf{x}) \to e^{2i\mathbf{K}\cdot\mathbf{u}(\mathbf{x})}(-\sigma^{2})\mu^{3}\tau^{1}\psi^{*}(\mathbf{x}),$$

$$\mathcal{M}_{x}: \quad \psi(\mathbf{x}) \to e^{i(\mathbf{K}'-\mathbf{K})\cdot\mathbf{u}(\mathcal{M}_{x}\mathbf{x})}W_{1}\psi(\mathcal{M}_{x}\mathbf{x}), \qquad (12)$$

$$R_{\frac{\pi}{2}}: \quad \psi(\mathbf{x}) \to e^{i(\mathbf{K}''-\mathbf{K})\cdot\mathbf{u}(R_{\frac{\pi}{2}}\mathbf{x})}W_{2}\psi(R_{\frac{\pi}{2}}\mathbf{x}),$$

$$\mathcal{T}: \quad \psi(\mathbf{x}) \to -\mu^{3}\tau^{3}\psi^{*}(\mathbf{x}), \quad i \to -i,$$

where $K' \equiv \mathcal{M}_x K$ and $K'' \equiv R_{\frac{\pi}{2}} K$. It turns out that K' = K''. For the symmetries \mathcal{M}_x and $R_{\frac{\pi}{2}}$, the deformation field must also undergo the transformation $u(x) \to \hat{O}^{-1} u(\hat{O}x)$. Here, the \mathcal{M}_x and $R_{\frac{\pi}{2}}$ actions on a vector \mathbf{v} are given by \mathcal{M}_x : $\mathbf{v} = (v_x, v_y) \to \mathcal{M}_x \mathbf{v} = (-v_x, v_y)$ and $R_{\frac{\pi}{2}} : \mathbf{v} = (v_x, v_y) \to R_{\frac{\pi}{2}} \mathbf{v} = (-v_y, v_x)$. The symmetry transformation law for ψ^{\dagger} 's can be obtained by taking the Hermitian conjugate on both sides of the transformation laws in Eqs. (12).

III. CONTINUUM MODEL FOR BILAYER STAGGERED-FLUX SQUARE LATTICE WITH GENERAL DEFORMATIONS

In this section, we consider two layers of staggered-flux square lattices with general deformations $u_t(x)$, $u_b(x)$ for the top and bottom layers, respectively. As pointed out in Ref. [55], one can start by considering the general form of interlayer tunneling:

$$H_1 = \int d^2 \mathbf{x} \ \psi_b^{\dagger}(\mathbf{x}) M[\mathbf{u}_t(\mathbf{x}), \mathbf{u}_b(\mathbf{x})] \psi_t(\mathbf{x}) + \text{H.c.}$$
 (13)

Here, $\psi_{t,b}$ refers to the Dirac fermions in the two layers of the staggered-flux square lattices with their subscripts the layer index. Each of ψ_t , ψ_b is an eight-component Dirac fermion with suppressed Dirac spinor, valley, and spin indices. In this paper, we assume spin-independent interlayer tunneling. Therefore, the interlayer tunneling matrix elements can be organized into a 4×4 matrix M that only act on the fourfold space labeled by the Dirac spinor index and the valley index. The form of Eq. (13) guarantees the locality of the interlayer tunneling, which is a natural expectation for the continuum model. All the subdominant terms depending on the gradients of the displacements and/or the gradients of the Dirac fermion fields $\psi_{t,b}$ have been omitted. Now we use the symmetries given in Eqs. (11) and (12) to bootstrap the general form of M.

A. Bootstrap

First, the deformation of both layers by a uniform vector should not change the interlayer physics. Therefore $M[u_t, u_b] = M[u_t - u_b] \equiv M[u]$, where $u \equiv u_t - u_b$. Second, deformation of a single layer by two lattice vectors should leave the physics invariant, which is due to the unit cell structure given by $\mathbf{R} = (R_x, R_y)$ with $R_{x,y}$ both even integers:

$$M[u] = M[u + 2\hat{x}] = M[u + 2\hat{y}],$$
 (14)

which leads to the Fourier expansion

$$M[u] = \sum_{k \in (\pi \mathbb{Z}, \pi \mathbb{Z})} e^{ik \cdot u} M_k. \tag{15}$$

Now, we consider the invariance of Eq. (13) under the simultaneous translation of both layers by one lattice spacing. For example, under the T_x of both layers, we have $\psi_b^{\dagger}M[u]\psi_t + \text{H.c.} \rightarrow \psi_b^t e^{-2iK \cdot u_b} \tau^1 \sigma^2 M[u] e^{2iK \cdot u_t} \sigma^2 \tau^1 \psi_t^* + \text{H.c.}$. The invariance of Eq. (13) requires the two expressions before and after the T_x transformation to be identical, namely, $M[u] = -e^{-2iK \cdot u} \tau^1 \sigma^2 M^*[u] \sigma^2 \tau^1$. In terms of the Fourier components

of M[u], the requirement imposed by T_x can be written as

$$T_x: M_{-k-2K} = -\tau^1 \sigma^2 M_k^* \sigma^2 \tau^1.$$
 (16)

Similarly, the interlayer tunneling Eq. (13) should also be invariant when both layers are simultaneously acted on by the symmetry actions T_y , \mathcal{M}_x , $R_{\frac{\pi}{2}}$, and \mathcal{T} . We can summarize all the symmetry constraints on the Fourier components of M[u] as

$$T_{x}: M_{-k-2K} = -\tau^{1}\sigma^{2}M_{k}^{*}\sigma^{2}\tau^{1},$$

$$T_{y}: M_{-k-2K} = -\tau^{1}\mu^{3}\sigma^{2}M_{k}^{*}\sigma^{2}\mu^{3}\tau^{1},$$

$$\mathcal{M}_{x}: M_{\mathcal{M}_{x}k+K'-K} = W_{1}^{\dagger}M_{k}W_{1},$$

$$R_{\frac{\pi}{2}}: M_{R_{\frac{\pi}{2}}k+K'-K} = W_{2}^{\dagger}M_{k}W_{2},$$

$$\mathcal{T}: M_{k} = -\tau^{3}\mu^{3}M_{k}\mu^{3}\tau^{3}.$$

$$(17)$$

Here, remember that $K' = \mathcal{M}_x K = R_{\frac{\pi}{2}} K$. In addition, we impose an extra symmetry S that exchanges the two layers: $\psi_t \leftrightarrow \psi_b$ and $u_t \leftrightarrow u_b$ (or, equivalently, $u \leftrightarrow -u$). The invariance of the interlayer tunneling under S leads to the additional constraint

$$S: \quad M_k = M_k^{\dagger}. \tag{18}$$

The set of conditions in Eqs. (17) and (18) relate the Fourier component M_k of M[u] with other Fourier components within the set $\{M_{k'} \mid k' = \mathcal{M}_x^m R_{\frac{\pi}{2}}^n (k+K) - K, m=0, 1, n=0, 1, 2, 3\}$ which contains either four or eight elements, depending on momentum k. In general, we expect that the Fourier components M_k decay rapidly for large |k|. As exemplified by the twisted bilayer graphene case, it should suffice to take the minimal set of Fourier components that contains the smallest allowed k and other symmetry-related Fourier components. (The general form of higher-momentum Fourier components M_k is discussed in Appendix.) In our case, the minimal set is given by $\{M_{k=0}, M_{-2K}, M_{K'-K}, M_{-K'-K}\}$ with k=0. The symmetry constraints require that

$$M_{k=0} = -M_{-2K} = w_1 \tau^1 + w_2 \mu^3 \tau^1 \equiv M_0,$$

$$M_{K'-K} = -M_{-K'-K} = w_1 \tau^2 - w_2 \mu^3 \tau^2 \equiv M_1,$$
 (19)

where the coupling constants w_1 and w_2 are both real numbers. Within the minimal set of Fourier components, the general form of interlayer tunneling is specified by

$$M[\mathbf{u}] = 2ie^{-i\mathbf{K}\cdot\mathbf{u}}[M_0\sin(\mathbf{K}\cdot\mathbf{u}) + M_1\sin(\mathbf{K}'\cdot\mathbf{u})]$$
 (20)

and the full continuum Hamiltonian of the deformed bilayer staggered-flux square lattice is given by Eqs. (10), (13), (20).

From Eq. (20), it is interesting to notice that in the case where two undeformed square-lattice layers are stacked on top of each other with no relative displacement, i.e., u = 0, the interlayer continuum Hamiltonian vanishes. In fact, this statement on the vanishing of M[u] at u = 0 is not just restricted to the minimal set of Fourier components (see Appendix for more details). It is satisfied even without any truncation in the Fourier components of M[u]. However, we would like to point out that M[u = 0] = 0 does not imply the vanishing of interlayer tunneling at the lattice scale. Rather, it means that the lattice-scale interlayer tunneling, if it exists, can at most

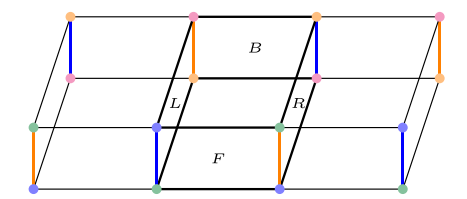


FIG. 3. The bilayer staggered-flux square lattice with a uniform relative deformation $(u_x, u_y) = (1, 0)$ is depicted. The blue, green, orange, and pink vertices correspond, respectively, to the lattices site indexed by i=1,2,3,4 following Eq. (3). In the horizontal plane, the unit cell of the bilayer system still covers two lattice spacings in both the x and y directions. There are four vertical plaquettes in each unit cell labeled F, B, L and R. There are four vertical links in each unit cell colored blue, green, orange, and pink. The interlayer tunneling only occurs along vertical links. See the main text for the tunneling strength along each link. The interlayer tunneling corresponds to having magnetic fluxes $2\Phi + 2\phi - \pi$, $-2\Phi - 2\phi + \pi$, $\pi - 2\Phi + 2\phi$, $-\pi + 2\Phi - 2\phi$ through the F, B, L, and R plaquettes, respectively.

lead to subdominant terms such as terms with derivatives of $\psi_{1,2}$ in the continuum theory. Here, we have made an implicit assumption that the lattice-scale interlayer tunneling is weak compared to the energy scale of the hopping within each layer. We will neglect the subdominant terms in the interlayer tunneling.

When u = 0, $u = \pm \hat{x}$, or $u = \pm \hat{y}$, the sites of the top layer are directly on top of the sites of the bottom layer. In the general setting where u depends on the spatial location, the factors $\sin(K \cdot u)$ and $\sin(K' \cdot u)$ of the interlayer tunneling Eq. (20) suggest that the most contribution to the interlayer tunneling comes from the regimes where u is locally close to $\pm \hat{x}$ or $\pm \hat{y}$. In Sec. III B, we will discuss the case with a uniform deformation where $u = \hat{x}$ is constant in space. The physical meaning of the parameters $w_{1,2}$ will become clear in this discussion. Other cases with $u = -\hat{x}$ or $\pm \hat{y}$ are similar to case of $u = \hat{x}$.

B. Uniform deformation

To gain some intuition of the interlayer tunneling term Eq. (20), we will first discuss the case in which the top layer is rigidly shifted along the x direction by one lattice spacing while the bottom layer is intact. In this case, the relative deformation u is uniform in space and is given by $u = \hat{x}$, namely, $(u_x, u_y) = (1, 0)$ in the unrotated coordinates (which can also be written as $u = (u_1, u_2) = (1, -1)/\sqrt{2}$ in the 45°-rotated coordinates). Rewritten in terms of the undeformed lattice positions R, the Lagrangian coordinates, the interlayer tunneling term is given by

$$H_1 = 2 \int d^2 \mathbf{R} \, \psi_b^{\dagger}(\mathbf{R}) (M_0 - M_1) \psi_t(\mathbf{R} + \mathbf{u}) + \text{H.c.}$$
 (21)

Transforming it back to the lattice fermions, the interlayer Hamiltonian can be understood via Fig. 3. Within the 2×2 unit cell of each layer, the four sites, which are labeled by i=1,2,3,4 in Eq. (3), are colored as blue, green, orange, and pink vertices, respectively. The spin-independent interlayer tunneling occurs between sites in the two layers that

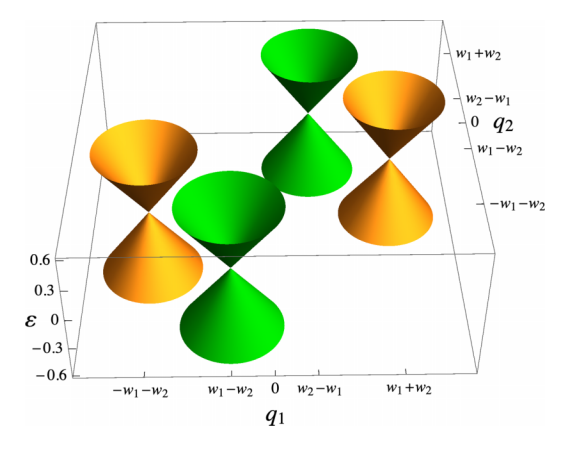


FIG. 4. The shifted Dirac cones at half filling for a uniform deformation $u = \hat{x}$. The two colors correspond to the two valleys $\mu^3 = \pm 1$.

are connected by vertical links. Depending on the color of the link shown in Fig. 3, the hopping terms are different. The amplitudes of the tunneling terms from the top to the bottom layer are given by (1) $2we^{-i\phi}$ for the blue links and (2) $2we^{i(\phi-\pi)}$ for the orange links. Here w is given by $w = |w_1 + iw_2|$, and $\phi = \arctan(w_2/w_1) + \pi/4$.

One can understand the interlayer tunneling terms as follows. The unit cell of this bilayer system in the horizontal plane is still 2×2 in lattice spacings. Each such unit cell contains four vertical plaquettes labeled as F, B, L, and R, respectively, as shown in Fig. 3. The interlayer tunneling terms described above correspond to having magnetic fluxes $2\Phi + 2\phi - \pi$, $-2\Phi - 2\phi + \pi$, $\pi - 2\Phi + 2\phi$, $-\pi + 2\Phi - 2\phi$ through the F, B, C, and C0 vertical plaquettes.

In this bilayer system, when the interlayer tunneling is turned off, i.e., $w_1 = w_2 = 0$, the band structure is gapless only at $\mathbf{q} = (0,0)$. The continuum theory equivalently describes 8 copies of two-component Dirac fermions. These eight copies come from twofold valley, twofold spin, and twofold layer degrees of freedom. As we turn on a finite interlayer tunneling w_1 and w_2 , one observes that the original gapless point at $\mathbf{q} = (0,0)$ splits into four gapless Dirac points located at $(q_1,q_2) = \pm (w_1 + w_2, w_2 - w_1), \pm (w_1 - w_2, -w_1 - w_2)$ in the 45°-rotated coordinates, see Fig. 4 below. Each of these Dirac points is described by two copies of two-component Dirac fermion with the two copies coming from the twofold spin degrees of freedom.

C. Rigid twist

Now we consider the case of a twisted bilayer staggered-flux square lattice where the two layers are deformed by rigid rotations by angles $\pm \theta/2$. We assume the twist angle θ is small. Hence, the deformation field can be written as $u_t = -u_b = \frac{\theta}{2}\hat{z} \times x$, where \hat{z} is the unit vector along the z direction. The interlayer tunneling can be obtained directly by plugging $u = \theta \hat{z} \times x$ in Eq. (20). The Hamiltonian terms within each of the top and bottom layers are obtained by plugging $u_{t/b}$ into Eq. (10). Here, we've also assumed that there is no chemical potential difference between the top and bottom layers. We note that the terms $\psi_t^{\dagger} \tau^j (\partial_j u_t^i) \partial_i \psi_t$ and $\psi_b^{\dagger} \tau^j (\partial_j u_b^i) \partial_i \psi_b$ that

capture the rotation of the Dirac cones in each layer each contains two derivatives and, hence, is parametrically small compared to other terms for small twist angle θ as the relevant physics happens at the moiré lattice length scale. We drop these two terms to simplify the Hamiltonian. One can further simplify the Hamiltonian by the redefining the fields $\psi_l(x) \to e^{iK \cdot u_l} \psi_l(x)$ for the two layers l = t, b. The continuum model Hamiltonian for the twisted bilayer staggered-flux square lattice now reads

$$H = \int d^2x \left\{ \sum_{l=t,b} \psi_l^{\dagger}(\mathbf{x}) (-i\tau^i \partial_i) \psi_l(\mathbf{x}) + (2i\psi_b^{\dagger}(\mathbf{x})[M_0 \sin(Ku_1) + M_1 \sin(Ku_2)] \psi_t(\mathbf{x}) + \text{H.c.}) \right\},$$
(22)

where $K=|K|=\pi/\sqrt{2}$ and $(u_1,u_2)=(-\theta x_2,\theta x_1)$ in the 45°-rotated coordinate. If we did not drop the terms $\psi_t^\dagger \tau^j (\partial_j u_t^i) \partial_i \psi_t$ and $\psi_b^\dagger \tau^j (\partial_j u_b^i) \partial_i \psi_b$ for each layer, we would need to do an extra layer-dependent rotation of the Dirac spinor $\psi_{t/b} \to e^{\mp i \tau^3 \theta/4} \psi_{t/b}$ to remove these terms from the Hamiltonian. Such a layer-dependent rotation in fact leaves the interlayer tunneling terms invariant. Hence, the Hamiltonian Eq. (22) is still valid even when the effect of the intralayer terms $\psi_t^\dagger \tau^j (\partial_j u_t^i) \partial_i \psi_t$ and $\psi_b^\dagger \tau^j (\partial_j u_b^i) \partial_i \psi_b$ are considered. Now using the identity $K \cdot u = Q \cdot x$ with $Q \equiv \theta(K \times \hat{z})$, M[u] can be further written as M(x). Moreover, we turn to the dimensionless parametrization $\tilde{q} = q/|Q|$, $\tilde{x} = |Q|x$ and $\tilde{w}_i = w_i/|Q|$. Combining all these and omitting the tildes from now on, we arrive at

$$H = \int d^2 \mathbf{x} \left\{ \sum_{l=t,b} \psi_l^{\dagger}(\mathbf{x}) (-i\tau^i \partial_i) \psi_l(\mathbf{x}) + \left(2i\psi_b^{\dagger}(\mathbf{x}) (-M_0 \sin x_2 + M_1 \sin x_1) \psi_t(\mathbf{x}) + \text{H.c.} \right) \right\},$$
(23)

Here we have also rescaled the energy by an overall of multiplicative factor. Notice from Eq. (19) that the two valleys (corresponding to $\mu^3 = \pm 1$) are decoupled. In the following, we will only focus on the $\mu^3 = +1$ valley as the spectrum of the $\mu^3 = -1$ valley follows straightforwardly by replacing $w_2 \to -w_2$. Focusing on the $\mu^3 = +1$ valley, we can effectively write $M_0 = (w_1 + w_2)\tau^1 \equiv w_s\tau^1$ and $M_1 =$ $(w_1 - w_2)\tau^2 \equiv w_a\tau^2$. We will present the analytical study of the Hamiltonian Eq. (23) in the next section. Before that, we comment on two special limits: (1) When $w_1 = \pm w_2$, we are in the chiral limit where either M_0 or M_1 vanishes and the interlayer interaction becomes uniform in either the x_1 or x_2 direction. In this case, the moiré superlattice is quasi-one-dimensional. (2) When $w_2 = 0$, the Hamiltonian is independent of the valley Pauli matrix μ and recovers the SU(4) symmetry (acting on the valley and spin spaces) of the decoupled-layer case.

We can numerically compute the spectrum of the Hamiltonian Eq. (23). We start by discussing the chiral limit. In the chiral limit, the system has continuous translation sym-

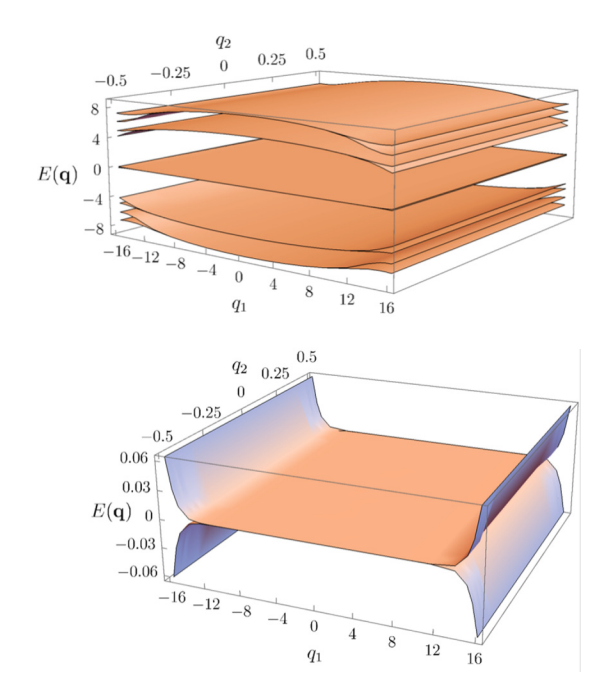


FIG. 5. Top panel: Band structures in the chiral limit $w_s = 10$, $w_a = 0$. The momentum q_1 is conserved while q_2 takes value in the moiré Brillouin zone $q_2 \in (-1/2, 1/2)$. Bottom panel: Zoomed-in view of the flattened bands (with the coupling constants w_a and w_s) near half filling.

metry along either the x_1 or the x_2 direction. For example, when $w_1 = w_2$, i.e., $w_a = 0$, the momentum q_1 along the x_1 direction is conserved, while the momentum q_2 , still being the crystal momentum along the x_2 direction, is conserved only modulo integer and, hence, has a Brillouin zone of [-1/2, 1/2). In Fig. 5, we show an example of the band structure in the chiral limit $w_a = 0$ and $w_s = 10$. Both the top and bottom panels correspond to the same parameters. In this band structure for which the valley index $\mu^3 = +1$ is already fixed, every band shown in Fig. 5 has a twofold degeneracy (in addition to the twofold spin degeneracy). From the top panel of Fig. 5, we notice that the two bands near the half filling are extremely flat and close to zero energy in a large area in the momentum space. The bottom panel of Fig. 5 shows the zoomed-in view of the two bands near half filling showing they are still dispersive bands whose energies are not exactly zero. The deviation from zero energy grows as the momentum q_1 increases. Here, we emphasize that there is in fact no gap separating the two bands near half filling from other bands. These two bands near half filling will overlap with other bands in energy for larger values of q_1 that are beyond the range plotted in Fig. 5. We will discuss the analytical understanding of the twofold degeneracy and the emergence of a large momentum-space region where the bands flatten in the next section. Also, we will show that the the entire spectrum must be free of gaps at any energy.

When we move away from the chiral limit, both momenta $q_{1,2}$ become crystal momenta defined within the moiré Brillouin zone, i.e., $q_{1,2} \in [-\pi, \pi)$. Figure 6 shows the single-valley band structures (with $\mu^3 = +1$) for various $w_s = 1, 1.4, 1.8, 3$ and a fixed $w_a = 0.5$. The plotted band structures are the band structure along a momentum-space

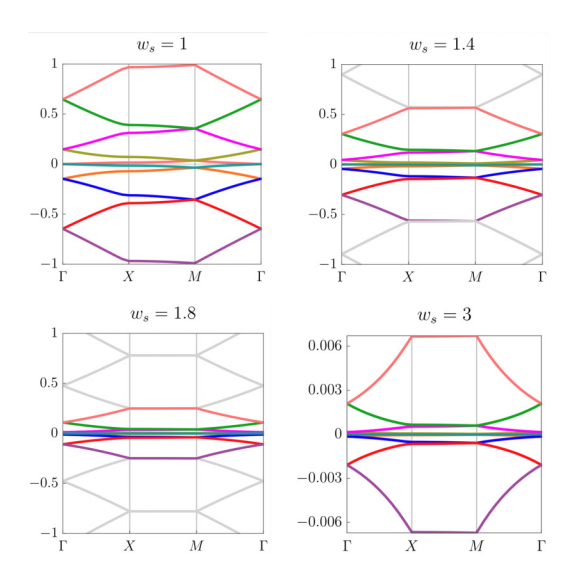


FIG. 6. Band structures along the moiré Brillouin zone trajectory $\Gamma \to X \to M \to \Gamma$ for various w_s 's with a fixed $w_a = 0.5$ is plotted. For fixed spin and valley indices, the spectrum is twofold degenerate [corresponding the quantum number $s = \pm 1$ in Eq. (24)]. All bands are connected by Dirac cones at the Γ and the M points in the moiré Brillouin zone. The ten bands (with each doubly degenerate) which are nearest to the zero energy are colored. As w_s increases, the spectrum is compressed toward the zero energy and the bands near zero-energy are flattened. Note that the energy range of the plot with $w_s = 3$ in the right bottom panel is about 200 times smaller than the other plots.

contour that connects the Γ point $(q_1, q_2) = (0, 0)$, the Xpoint $(q_1, q_2) = (\pi, 0)$, and the *M* point $(q_1, q_2) = (\pi, \pi)$. Similar to the chiral limit, each band is twofold degenerate in addition to the twofold spin degeneracy. In Fig. 6, the colored bands are the ten bands that are closest to zero energy. We see that, as w_s increases, the spectrum gets compressed toward zero energy and the bands near zero energy flattened, which yields a large number of low-energy states. We also notice that each band is connected with its neighboring bands via Dirac cones at the Γ point or at the M point. Hence, the entire band structure is infinitely connected and free of band gaps at all energies. We will discuss the twofold degeneracy of each band, the flattening of the bands near zero energy, and the infinite connectivity of the bands in the next section. We will also discuss the analytical understanding of the infinite connectivity of the bands shown in Fig. 6.

IV. ANALYTICAL STUDY OF THE MAGIC CONTINUUM

In this section, we discuss the magic continuum of the twisted bilayer staggered-flux square lattice where the two layers are deformed by rigid rotations of angles $\pm\theta/2$, respectively. As discussed in Sec. III C, upon the field redefinition and the rescaling of momentum and energy, the Hamiltonian of this twisted bilayer is given by Eq. (23). As explained above, it suffices to focus only on the $\mu^3=+1$ valley. We notice that the problem can be further simplified using the following basis of the single-particle wave function:

$$\begin{pmatrix} \psi_t \\ \psi_b \end{pmatrix} = \frac{1}{\sqrt{2}} \begin{pmatrix} \psi \\ is\psi \end{pmatrix}. \tag{24}$$

The Hamiltonian Eq. (23) of the twisted bilayer system is diagonal in the $s = \pm 1$ basis. We would like to comment that, as shown in Appendix, s is always a good quantum number in the twisted bilayer system, even when we consider the most general form of spin-independent interlayer tunneling M[u] (including the Fourier components beyond the minimal set) allowed by the constraints discussed in Sec. III A. In the following discussions, we will still focus on the Hamiltonian Eq. (23) where the interlayer tunneling involves the minimal and most dominant set of Fourier components. Physically, the quantum number s can be understood as inherited from the spatial regions where u is locally close to $u = \pm \hat{x}$ and $u = \pm \hat{y}$ and where the interlayer tunneling acquires most of its contribution from. In these spatial regions, each combination of the quantum number $s = \pm 1$ and the valley index $\mu^3 = \pm 1$ is locally associated with one of the four Dirac cones shown in Fig. 4 (obtained with the uniform deformation). For a given quantum number s (and the fixed valley index $\mu^3 = 1$), the single-particle Hamiltonian that acts on ψ

$$h = \tau^{1}(-i\partial_{1} - 2sw_{s}\sin x_{2}) + \tau^{2}(-i\partial_{2} + 2sw_{a}\sin x_{1}).$$
 (25)

This Hamiltonian equivalently describes a Dirac fermion in a periodically modulated effective background magnetic field $B(\mathbf{x}) = 2s(w_a \cos x_1 + w_s \cos x_2)$ written in a Coulomb gauge. The problem of Dirac fermion in an effective periodic magnetic field has been shown to emerge and has been investigated in the contexts of strained graphene [59,60], graphene in a field [61,62], and strained topological crystalline insulators [63]. As a brief remark, our analysis has been focusing on the limit $t/\Delta = 1$ where the continuum description of the single-layer theory Eq. (6) has an isotropic Dirac velocity. When we take $t/\Delta \neq 1$ in Eq. (1), namely, when the Dirac velocity of the single-layer theory develops a valley-dependent anisotropy, the above Eq. (25) would only get modified by a valley-dependent velocity anisotropy. The terms induced by the interlayer tunneling remain intact and all the analyses below can still carry over. Hence, we will continue the analysis in the isotropic limit in the following.

In this section, we will discuss the exponential reduction of the Dirac velocity in the Hamiltonian Eq. (25), the emergence of flattened bands and the associated large number of lowenergy states in the magic continuum. We will also discuss the analytical understanding of the infinite connectivity of all the bands shown in Fig. 6.

A. Exact zero-energy states at the Dirac point and the renormalized Dirac velocity

Similar to the twisted bilayer graphene system, the band structure of the twisted bilayer staggered-flux square lattice contains Dirac cones near half filling inherited from each of the staggered-flux square-lattice layers. The location of the inherited Dirac points in the twisted bilayer system should be at $(q_1, q_2) = (0, 0)$ for the Hamiltonian Eq. (25).

The zero-energy eigenstates exactly at the Dirac point can be solved analytically. Notice that the zero-energy eigenstates of h in Eq. (25) should also be the eigenstates of τ^3 . The analytical expression of the exact zero-energy eigenstates are

given as

$$\psi_{+} = c_{+} {e^{-B(x)} \choose 0}, \quad \psi_{-} = c_{-} {0 \choose e^{B(x)}},$$
 (26)

where c_{\pm} are the normalization constants which can be fixed by integrating over the moiré unit cell:

$$c_{+} = c_{-} = \left[4\pi^{2} I_{0}(4w_{s}) I_{0}(4w_{a})\right]^{-1/2}.$$
 (27)

Here I_0 is the modified Bessel function of the first kind. Notice that the exact zero-energy eigenstates ψ_{\pm} satisfy the periodic condition that

$$\psi_{\pm}(x_1, x_2) = \psi_{\pm}(x_1 + 2\pi, x_2) = \psi_{\pm}(x_1, x_2 + 2\pi),$$
 (28)

which is in agreement with the expectation that the Dirac point of the bilayer system is located at $(q_1, q_2) = (0, 0)$ within the moiré Brillouin zone. One can also prove that these solutions are unique.

We now compute the Dirac velocity. In momentum space, ψ_{\pm} are the eigenstates solutions at the Dirac point $(q_1, q_2) = 0$. The effective single-particle Hamiltonian for small q near q = (0,0) can be obtained by treating the term $q_i \tau^i$ as a perturbation to the subspace formed by the solutions ψ_{\pm} at q = 0. The matrix elements of the perturbation $q_i \tau^i$ are given by

$$h_{q,\xi\xi'} = \int_{u.c.} d^2 x \, \psi_{\xi}^{\dagger}(x) (\tau^i q_i) \psi_{\xi'}(x), \tag{29}$$

where $\xi, \xi' = \pm$ and $\int_{u.c.} d^2x$ denotes the integration over a moiré unit cell (in the real space). Here $\psi_{\xi'}$ and $\psi_{\xi'}^{\dagger}$ represents the wave function $\psi_{\pm}(x)$ and their conjugate, which should not be confused with fermion operators. Plugging in the expressions Eqs. (26) and (27), we arrive at

$$h_{q} = \tau^{i} q_{i} / I_{0}(4w_{a}) I_{0}(4w_{s}), \tag{30}$$

which captures the dispersion of the bands near zero energy in the vicinity of $\mathbf{q}=(0,0)$. Equation (30) describes a gapless Dirac cone with a renormalized Dirac velocity. A similar analysis of the renormalization of the Dirac velocity was also given in Ref. [61] which studied a monolayer graphene under general periodic magnetic and electric fields.

From Eq. (30), the renormalized Dirac velocity is given by

$$v^* = 1/I_0(4w_a)I_0(4w_s). (31)$$

We are interested in how v^* changes as the coupling constants w_a and w_s vary. The function $I_0(z)$ satisfies $I_0(0)=1$ and increases monotonically and exponentially with |z|. When $w_s=w_a=0$, $v^*=1$ recovers the results for the decoupled bilayer. As $|w_s|$ and/or $|w_a|$ increase, the Dirac velocity v^* becomes exponentially suppressed. At the same time, the bands near half filling are flattened, leading to a large number of near-zero-energy states. This exponential suppression of the Dirac velocity and the emergence of flattened bands occur in a very large range of w_a and w_s , which is in contrast to the twisted bilayer graphene system where the drastic reduction of the Dirac velocity and bandwidth only occurs around a discrete set of coupling constants and twist angles. Hence, there is a magic continuum in the twisted bilayer staggered-flux square lattice system.

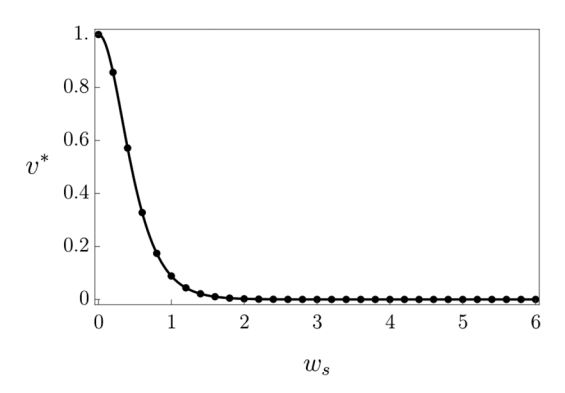


FIG. 7. The renormalized Dirac velocity v^* as a function of w_s in the chiral limit $w_a = 0$. There is a magic continuum for $w_s \gtrsim 1$. The dots are the numerically computed Dirac velocity. The smooth line is the modified Bessel function $I_0(4w_s)^{-1}$, which is the analytical expression of the reduced Dirac velocity v^* we obtained in Eq. (31).

In Fig. 7, we plot the Dirac velocity v^* as a function of w_s obtained from numerically computing the spectrum, which shows a perfect match with the analytical expression above. For simplicity, we've only focused on the chiral limit $w_a = 0$ where q_1 is conserved in Fig. 7. The expression of the renormalized Dirac velocity Eq. (31) is generally applicable for any parameters w_a and w_s .

B. Intuitive understanding of the emergence of a large number of low-energy bands

In this subsection, we provide an intuitive understanding of the emergence of a large number of low-energy bands as w_a and w_s increase. Here, by low-energy bands, we refer to the bands with energies close to zero, namely, close to half filling. Recall that in a uniform magnetic field of strength B, the massless Dirac fermions form a set of Landau levels. Each quantum state occupies an area of $2\pi l_B^2$ with $l_B=1/\sqrt{B}$ the magnetic length, and the degeneracy of each Landau level is the ratio of the full area of the system divided by $2\pi l_B^2$. For a spatial region with a finite size, the Landau-level degeneracy can be well-approximated by the number of magnetic flux quanta contained in this region (regardless of the sign of the magnetic field). For a review, see, for example, Ref. [64].

When the magnetic field is slowly varying over l_B , the Landau levels remain a good approximation. But the Landau levels will have position-dependent energies

$$E_n(\mathbf{x}) = \pm \sqrt{2n|B(\mathbf{x})|},\tag{32}$$

where $n \in \mathbb{Z}$ labels the different Landau levels. Because of the dependence on x, Landau levels at different positions are no longer degenerate and collectively form dispersive bands. The n=0 Landau level is rather special as its energy does not depend on B(x). However, the chirality [labeled by the \pm signs in Eq. (32)] of the Landau level depends on the sign of B(x). For the twisted bilayer staggered-flux square lattice, the effective magnetic field $B(x) = 2s(w_a \cos x_1 + w_s \cos x_2)$ has a spatially dependent sign. Therefore, different spatial regions will host the n=0 Landau level of opposite chiralities, which yields dispersive modes on the interfaces between these regions and also perturbs the states in the local n=0

Landau level away from exactly zero energy. Even though the state in the local n = 0 Landau level will no longer have exactly zero energy, their energies will still remain close to zero when the local magnetic length is much smaller than the length scale of variation of B(x). To make an estimate of the number of states with energy close to zero, we first divide a spatial moiré unit cell, which can be chosen as $(x_1, x_2) \in [-\pi/2, 3\pi/2) \times [-\pi/2, 3\pi/2)$, into four subregions $A_1 = [-\pi/2, \pi/2) \times [-\pi/2, \pi/2)$, $A_2 = [\pi/2, 3\pi/2) \times [-\pi/2, \pi/2), \quad A_3 = [-\pi/2, \pi/2) \times$ $[\pi/2, 3\pi/2)$ and $A_4 = [\pi/2, 3\pi/2) \times [\pi/2, 3\pi/2)$, whose centers are the four local extrema of B(x). For every subregion, we replace the effective magnetic field B(x) by its average value in the same subregion. With this replacement, the numbers of magnetic flux quanta through subregions A_1 and A_4 are both $2|w_s + w_a| = 4|w_1|$, while the numbers of flux quanta through A_2 and A_3 are both $2|w_s - w_a| = 4|w_2|$. Their sum is proportional, $|w_1| + |w_2|$, and gives an estimate for the number of close-to-zero-energy state in a moiré unit cell. Therefore, the number of close-to-zero-energy moiré bands in the band structure of the Hamiltonian Eq. (25) should be $\propto (|w_1| + |w_2|)$.

Note that the estimation above relies on the slow variation of the B(x) field on the scale of the local magnetic length, which amounts to the requirement that both $|w_1|, |w_2| \gg 1$. If we only have $|w_1| \gg 1$ but $|w_2|$ is small, then the earlier estimations in the A_2 and A_3 subregions won't be controlled while the arguments for A_1 and A_4 still work. Therefore, the degeneracy in this case is at least proportional to $|w_1|$. Similar arguments follow for the case with $|w_2| \gg 1$ and $|w_1|$ small.

We can compare the analysis above with numerical calculations. This band structure is free of a band gap. To numerically estimate the number of low-energy bands in the system, we have to choose a specific small energy window around zero energy and only count the number of (numerically obtained) bands fully contained inside this energy window. In Fig. 8, we plot the the numerically calculated number of moiré bands fully contained within the small energy window $E \in (-0.05, 0.05)$ as a function of $|w_1| + |w_2|$. Figure 8 exhibits a linear behavior in the parameter regime $|w_1|, |w_2| \gtrsim 1$, consistent with the previous analysis. If we change the size of the energy window, the number of bands within the energy window remains linearly dependent on $|w_1| + |w_2|$ but with a different slope.

C. Infinite band connectivity

The band structure shown in Fig. 6 is free of band gaps. All the bands are connected to each other. In this subsection, we show that this infinite connectivity of the band structure is demanded by the symmetry of the Hamiltonian Eq. (25). The first relevant symmetry is the original twofold spatial rotation symmetry $R_{\frac{\pi}{2}}^2: x_{1,2} \to -x_{1,2}, \ \psi(x) \to -\tau^z \psi(R_{\frac{\pi}{2}}^2x)$. For a fixed quantum number s (as well as a fixed valley index $\mu^3 = \pm 1$ and a fixed spin species), the Hamiltonian Eq. (25) is invariant under a new symmetry action $\tilde{R}_{\pi}\tilde{T}$ that combines a twofold spatial rotation $\tilde{R}_{\pi}: x_{1,2} \to -x_{1,2} + \pi$, $\psi(x) \to \psi(\tilde{R}_{\pi}x)$ and a time-reversal transformation $\tilde{T}: \psi(x) \to \tau^1 \psi(x)$, $\tau^1 \to -i$. Note that the symmetries \tilde{R}_{π} and \tilde{T} are different from the twofold spatial rotation symmetry

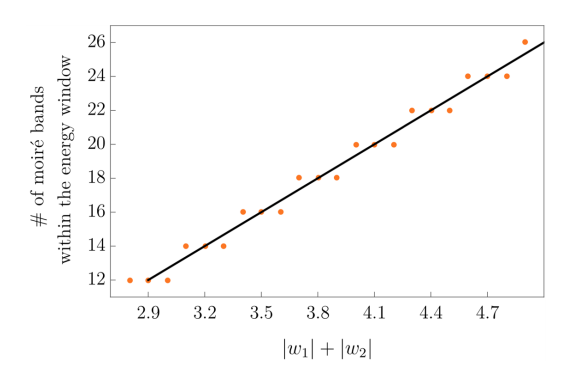


FIG. 8. Number of moiré bands with nearly zero energies scales linearly with $|w_1| + |w_2|$ in the regime with $|w_1|, |w_2| \gtrsim 1$. We fix $|w_1| - |w_2| = 1$ in the plot and count all the bands (obtained from numerical calculations) that completely lie within the energy window $E \in (-0.05, 0.05)$. Note that bands only partially lying inside the energy window are not included in the counting. The steplike feature is due to the fact that the number of moiré bands counted has to be an integer. The distance between steps is always two due to the fact that the spectrum is symmetric in energy about the E=0 axis. The black straight line is obtained from connecting the middle points of each step.

 $R_{\frac{\pi}{2}}^2$ and the time-reversal symmetry \mathcal{T} originating from the single-layer model of the staggered-flux square lattice. Each of \tilde{R}_{π} and $\tilde{\mathcal{T}}$ individually is not a symmetry of the Hamiltonian Eq. (25), but their combination $\tilde{R}_{\pi}\tilde{\mathcal{T}}$ is. The symmetry $\tilde{R}_{\pi}\tilde{\mathcal{T}}$ squares to 1, namely, $(\tilde{R}_{\pi}\tilde{\mathcal{T}})^2 = 1$.

For every band, this symmetry $\tilde{R}_{\pi}\tilde{T}$ ensures that the Berry curvature vanishes at every momentum point where the band structure (with the valley index μ^3 , the spin index and the quantum number s all fixed) is nondegenerate. At a generic degenerate point q, we expect the band structure to be locally described by a gapless Dirac cone which leads to a δ -function contribution to the Berry curvature with a total flux π fully concentrated at the momentum q. In general, the $\tilde{R}_{\pi}\tilde{T}$ symmetry allows δ functions in the Berry curvature with fluxes $n\pi$, $n \in \mathbb{Z}$ at a degenerate point. When |n| > 1, such a degenerate point can be generically split into |n| gapless Dirac cones without breaking the $\tilde{R}_{\pi}\tilde{\mathcal{T}}$ symmetry. For an isolated gapless Dirac cone, the symmetry $\tilde{R}_{\pi}\tilde{\mathcal{T}}$ forbids a nonzero Dirac mass and, hence, ensures the stability of the gapless Dirac cone. The constraint on the Berry curvature imposed by $\tilde{R}_{\pi}\tilde{T}$ leads to the consequence that each band must contain an even number of gapless Dirac points to ensure that total Berry flux within a band is an integer multiple of 2π . Since the Hamiltonian Eq. (25) also respects the twofold spatial rotation symmetry R_{π}^2 , gapless Dirac points must come in pairs in the moiré Brillouin zone except at the Γ point and M point. In other words, the symmetries $\tilde{R}_{\pi}\tilde{\mathcal{T}}$ and $R_{\frac{\pi}{2}}^2$ together require that the total number of gapless Dirac cones located at the Γ point and M point for each band has to be even.

Now, let's label the bands of the Hamiltonian Eq. (25) by $m = \pm 1, \pm 2, \ldots$ The band with label m > 0 (m < 0) is the |m|th band above (below) zero energy. Consider starting with vanishing $w_{a,s}$ and gradually turning them on. In the limit where $w_{a,s}$ are zero, the band m = 1 and the band m = -1 are connected via a single gapless Dirac cone centered at the

 Γ point. As we gradually turn on $w_{a,s}$, this gapless Dirac cone between the bands m=1 and m=-1 is stable and is pinned at zero energy by the time-reversal symmetry \mathcal{T} . At the M point, the bands m=1 and m=-1 are well separated in energy. To ensure that the m=1 band contains an even number of gapless Dirac points in total, it has to be connected to the m=2 band via a gapless Dirac cone located at the M point. Now, the requirement that the m=2 band contains an even number of gapless Dirac points further enforces a Dirac point at the Γ point connecting the m=2 and the m=3 bands. By iterating similar arguments, we can conclude that all the bands of the Hamiltonian Eq. (25) are connected via gapless Dirac cones at the Γ point and the M point.

The arguments above for the infinite connectivity of the bands in Eq. (25) rely on the symmetry $\tilde{R}_{\pi}\tilde{\mathcal{T}}$. The Hamiltonian Eq. (25) is obtained from choosing the minimal set of Fourier components in the interlayer tunneling M[u]. In Appendix A, we show that the symmetry $\tilde{R}_{\pi}\tilde{\mathcal{T}}$ is present even when we consider the most general form of spin-independent interlayer tunneling M[u] allowed by the constraints discussed in Sec. III A. Hence, the infinite connectivity of the bands is present under the general allowed spin-independent interlayer tunneling M[u].

V. DISCUSSION

To test the robustness of the our analysis, one can explicitly break certain microscopic symmetries. For example, when the reflection symmetry \mathcal{M}_x is broken, the terms $w_3\tau^2 + w_4\mu^3\tau^2$ can be added to M_0 in Eq. (19), while $-w_3\tau^1 + w_4\mu^3\tau^1$ can be added to M_1 in Eq. (19), with w_3 , w_4 both real. The Hamiltonian for the twisted bilayer staggered-flux square lattice system can again be understood as describing a massless Dirac Hamiltonian in the same periodic effective magnetic field, but in a different gauge for the corresponding vector potential. Similar properties are found if the rotation symmetry $R_{\frac{\pi}{2}}$ is broken while $R_{\frac{\pi}{2}}^2$ is still preserved. We've also checked that breaking only the time-reversal symmetry \mathcal{T} does not change the Hamiltonian for the twisted bilayer system when interlayer tunneling M[u] only involves its minimal set of Fourier components. However, lifting the constraints enforced by time-reversal symmetry \mathcal{T} and the layer-exchange symmetry S will enable additional $i(w_5\tau^0 + w_6\mu^3\tau^0)$ terms in M_0 , as well as the other corresponding terms in the M_k 's that are related to M_0 by spatial symmetries. With these additional terms, the original zero-energy Dirac cones will be gapped out. Note that the discussion here in this paragraph is restricted to the twisted bilayer system where the interlayer tunneling M[u] only includes its minimal set of the Fourier components. It would also be interesting to explore the effect of highermomentum Fourier components (beyond the minimal set) in the interlayer tunneling.

In this paper, we have studied the case of the twisted-bilayer staggered-flux square lattice. The staggered-flux square lattice was initially introduced to characterize the mean-field band structure of spinons in an algebraic spin liquid. It would be interesting to consider bilayer systems with each layer describing the spinon band structure of other spin liquid candidates. In different spin liquids, the spinon bands has different symmetry properties. When it comes to a bilayer system with arbitrary elastic deformations in each layer,

one can generalize the symmetry-based analysis to bootstrap the general form of interlayer tunneling for different spinon bands

Our study paves the path toward understanding the twisted bilayer spin liquid with dynamical U(1) gauge field. For a spin liquid, it is a common wisdom that when there is only a small number of flavors of Dirac fermions in the spinon band structure, the monopoles of the dynamical gauge field have a tendency to drive the system into a confined phase. But with the extremely flat bands of the spinons derived in this work, the large density of states of the spinons at low energy might render the monopoles much less influential. Hence, deconfinement of spinon might happen over a large length scale if the physics discussed in this paper is ever realized in real twisted magnetic materials.

ACKNOWLEDGMENTS

Z.-X.L. is supported by the Simons Collaborations on Ultra-Quantum Matter, Grant No. 651440 (LB) from the Simons Foundation. We thank Leon Balents for helpful discussions. C.X. is supported by NSF Grant No. DMR-1920434 and the Simons Foundation. Z.-X.L. is grateful to Michael Hermele and Jason Alicea for explaining their earlier works. C.-M.J. thanks Biao Lian for helpful discussion on band connectivity.

APPENDIX: GENERAL FORM OF SPIN-INDEPENDENT INTERLAYER TUNNELING

As discussed in Sec. III A, the conditions in Eqs. (17) and (18) relate the Fourier component M_k of the interlayer tunneling M[u] with other Fourier components within the set $\{M_{k'} \mid k' = \mathcal{M}_x^m R_{\frac{n}{2}}^n (k + K) - K, m = 0, 1, n = 0, 1, 2, 3\}$ which contains either four or eight elements depending on the momentum k. There is no constraint that relates the Fourier components of M[u] in different sets. Remember that the momentum k of the Fourier component M_k is restricted to $k \in (\pi \mathbb{Z}, \pi \mathbb{Z})$ in the unrotated coordinate as shown in Eq. (15).

When all momenta $\mathcal{M}_{x}^{m}R_{\frac{\pi}{2}}^{n}(\boldsymbol{k}+\boldsymbol{K})-\boldsymbol{K}$ for m=0,1 and n=0,1,2,3 are different, the set $\{M_{\boldsymbol{k}'}\,|\,\boldsymbol{k}'=\mathcal{M}_{x}^{m}R_{\frac{\pi}{2}}^{n}(\boldsymbol{k}+\boldsymbol{K})-\boldsymbol{K},m=0,1,n=0,1,2,3\}$ contains eight different Fourier components of $M[\boldsymbol{u}]$. The most general spin-independent solution to the constraints in Eqs. (17) and (18) is given by

$$M_{k} = w_{k,1}\tau^{1} + w_{k,3}\tau^{2} + w_{k,2}\tau^{1}\mu^{3} + w_{k,4}\tau^{2}\mu^{3},$$

$$M_{R_{\frac{\pi}{2}}(k+K)-K} = -w_{k,3}\tau^{1} + w_{k,1}\tau^{2} + w_{k,4}\tau^{1}\mu^{3} - w_{k,2}\tau^{2}\mu^{3},$$

$$M_{R_{\frac{\pi}{2}}^{2}(k+K)-K} = -w_{k,1}\tau^{1} - w_{k,3}\tau^{2} - w_{k,2}\tau^{1}\mu^{3} - w_{k,4}\tau^{2}\mu^{3},$$

$$M_{R_{\frac{\pi}{2}}^{3}(k+K)-K} = w_{k,3}\tau^{1} - w_{k,1}\tau^{2} - w_{k,4}\tau^{1}\mu^{3} + w_{k,2}\tau^{2}\mu^{3},$$

$$M_{\mathcal{M}_{x}(k+K)-K} = w_{k,3}\tau^{1} + w_{k,1}\tau^{2} - w_{k,4}\tau^{1}\mu^{3} - w_{k,2}\tau^{2}\mu^{3},$$

$$M_{\mathcal{M}_{x}(k+K)-K} = w_{k,1}\tau^{1} - w_{k,3}\tau^{2} + w_{k,2}\tau^{1}\mu^{3} - w_{k,4}\tau^{2}\mu^{3},$$

$$M_{\mathcal{M}_{x}R_{\frac{\pi}{2}}^{2}(k+K)-K} = -w_{k,1}\tau^{1} - w_{k,1}\tau^{2} + w_{k,4}\tau^{1}\mu^{3} + w_{k,2}\tau^{2}\mu^{3},$$

$$M_{\mathcal{M}_{x}R_{\frac{\pi}{2}}^{3}(k+K)-K} = -w_{k,1}\tau^{1} + w_{k,3}\tau^{2} - w_{k,2}\tau^{1}\mu^{3} + w_{k,4}\tau^{2}\mu^{3},$$

$$M_{\mathcal{M}_{x}R_{\frac{\pi}{2}}^{3}(k+K)-K} = -w_{k,1}\tau^{1} + w_{k,3}\tau^{2} - w_{k,2}\tau^{1}\mu^{3} + w_{k,4}\tau^{2}\mu^{3},$$

$$(A1)$$

where $w_{k,1}$, $w_{k,2}$, $w_{k,3}$, and $w_{k,4}$ are real parameters that are not subject to further constraints.

The situation in which the set $\{M_{k'} | k' = \mathcal{M}_x^m R_{\frac{\pi}{2}}^n (k + K) - K, m = 0, 1, n = 0, 1, 2, 3\}$ contains only four different Fourier components of M[u] occurs only when $M_x(k + K) = R_{\frac{\pi}{2}}(k + K)$ or $M_x(k + K) = R_{\frac{\pi}{2}}(k + K)$. When $M_x(k + K) = R_{\frac{\pi}{2}}(k + K)$, the solution to the constraints in Eqs. (17) and (18) is still given by Eq. (A1) but with an extra condition that

$$w_{k,3} = w_{k,4} = 0. (A2)$$

The minimal set of Fourier components of M[u] discussed in Sec. III A, which is the case with k = 0, exactly fits into this situation. When $M_x(k + K) = R^3_{\frac{\pi}{2}}(k + K)$, the solution is given by Eq. (A1) but with an extra condition that

$$w_{k,1} = w_{k,2} = 0. (A3)$$

Notice that the general form of the spin-independent interlayer tunneling that satisfies the conditions Eqs. (17) and (18) allows us to rewrite the Fourier expansion of

M[u] as

$$M[u] = \sum_{k \in (\pi \mathbb{Z}, \pi \mathbb{Z})} e^{ik \cdot u} M_k$$
$$= e^{-iK \cdot u} \sum_{k \in (\pi \mathbb{Z}, \pi \mathbb{Z})} i \sin((k + K) \cdot u) M_k.$$
(A4)

This form of M[u] ensures that when u = 0, namely, when the two layers of square lattices are not displaced relative to each other, the spin-independent interlayer tunneling vanishes. Also, we notice that the valley index $\mu^3 = \pm 1$ is a good quantum number under the most general spin-independent interlayer tunneling allowed by the conditions Eqs. (17) and (18). In the case where the two layers are rigidly twisted by a relative angle θ , by knowing that M_k 's are all Hermitian in Eq. (A4), we can show straightforwardly that the quantum number s introduced in Eq. (24) is also always a good quantum under the general form of M[u]. When both μ^3 and s are good quantum numbers, we can study the Hamiltonian of the twisted bilayer with both of them fixed like we did in Eq. (25). The general form of M[u] still preserves the $\tilde{R}_{\pi}\tilde{T}$ symmetry. Hence, the band structure for a fixed valley index μ^3 and a fixed quantum number s still has infinite connectivity.

- [1] Y. Cao, V. Fatemi, A. Demir, S. Fang, S. L. Tomarken, J. Y. Luo, J. D. Sanchez-Yamagishi, K. Watanabe, T. Taniguchi, E. Kaxiras, R. C. Ashoori, and P. Jarillo-Herrero, Nature (London) 556, 80 (2018).
- [2] Y. Cao, V. Fatemi, S. Fang, K. Watanabe, T. Taniguchi, E. Kaxiras, and P. Jarillo-Herrero, Nature (London) **556**, 43 (2018).
- [3] M. Yankowitz, S. Chen, H. Polshyn, Y. Zhang, K. Watanabe, T. Taniguchi, D. Graf, A. F. Young, and C. R. Dean, Science 363, 1059 (2019).
- [4] A. L. Sharpe, E. J. Fox, A. W. Barnard, J. Finney, K. Watanabe, T. Taniguchi, M. A. Kastner, and D. Goldhaber-Gordon, Science 365, 605 (2019).
- [5] X. Lu, P. Stepanov, W. Yang, M. Xie, M. A. Aamir, I. Das, C. Urgell, K. Watanabe, T. Taniguchi, G. Zhang, A. Bachtold, A. H. MacDonald, and D. K. Efetov, Nature (London) 574, 653 (2019).
- [6] M. Serlin, C. L. Tschirhart, H. Polshyn, Y. Zhang, J. Zhu, K. Watanabe, T. Taniguchi, L. Balents, and A. F. Young, Science 367, 900 (2020).
- [7] A. Kerelsky, L. J. McGilly, D. M. Kennes, L. Xian, M. Yankowitz, S. Chen, K. Watanabe, T. Taniguchi, J. Hone, C. Dean, A. Rubio, and A. N. Pasupathy, Nature (London) 572, 95 (2019).
- [8] Y. Xie, B. Lian, B. Jäck, X. Liu, C.-L. Chiu, K. Watanabe, T. Taniguchi, B. A. Bernevig, and A. Yazdani, Nature (London) 572, 101 (2019).
- [9] Y. Jiang, X. Lai, K. Watanabe, T. Taniguchi, K. Haule, J. Mao, and E. Y. Andrei, Nature (London) 573, 91 (2019).
- [10] S. Carr, D. Massatt, S. Fang, P. Cazeaux, M. Luskin, and E. Kaxiras, Phys. Rev. B 95, 075420 (2017).
- [11] K. Tran, G. Moody, F. Wu, X. Lu, J. Choi, K. Kim, A. Rai, D. A. Sanchez, J. Quan, A. Singh, J. Embley, A. Zepeda, M. Campbell, T. Autry, T. Taniguchi, K. Watanabe, N. Lu, S. K.

- Banerjee, K. L. Silverman, S. Kim *et al.*, Nature (London) **567**, 71 (2019).
- [12] C. Jin, E. C. Regan, A. Yan, M. I. B. Utama, D. Wang, S. Zhao, Y. Qin, S. Yang, Z. Zheng, S. Shi, K. Watanabe, T. Taniguchi, S. Tongay, A. Zettl, and F. Wang, Nature (London) 567, 76 (2019).
- [13] K. L. Seyler, P. Rivera, H. Yu, N. P. Wilson, E. L. Ray, D. G. Mandrus, J. Yan, W. Yao, and X. Xu, Nature (London) 567, 66 (2019)
- [14] E. M. Alexeev, D. A. Ruiz-Tijerina, M. Danovich, M. J. Hamer, D. J. Terry, P. K. Nayak, S. Ahn, S. Pak, J. Lee, J. I. Sohn, M. R. Molas, M. Koperski, K. Watanabe, T. Taniguchi, K. S. Novoselov, R. V. Gorbachev, H. S. Shin, V. I. Fal'ko, and A. I. Tartakovskii, Nature (London) 567, 81 (2019).
- [15] Y. Tang, L. Li, T. Li, Y. Xu, S. Liu, K. Barmak, K. Watanabe, T. Taniguchi, A. H. MacDonald, J. Shan, and K. F. Mak, Nature (London) 579, 353 (2020).
- [16] E. C. Regan, D. Wang, C. Jin, M. I. B. Utama, B. Gao, X. Wei, S. Zhao, W. Zhao, Z. Zhang, K. Yumigeta, M. Blei, J. D. Carlström, K. Watanabe, T. Taniguchi, S. Tongay, C. Michael, A. Zettl, and F. Wang, Nature (London) 579, 359 (2020).
- [17] Y. Shimazaki, I. Schwartz, K. Watanabe, T. Taniguchi, M. Kroner, and A. Imamoglu, Nature (London) 580, 472 (2020).
- [18] L. Wang, E.-M. Shih, A. Ghiotto, L. Xian, D. A. Rhodes, C. Tan, M. Claassen, D. M. Kennes, Y. Bai, B. Kim, K. Watanabe, T. Taniguchi, X. Zhu, J. Hone, A. Rubio, A. N. Pasupathy, and C. R. Dean, Nat. Mater. 19, 861 (2020).
- [19] X. Liu, Z. Hao, E. Khalaf, J. Y. Lee, Y. Ronen, H. Yoo, D. H. Najafabadi, K. Watanabe, T. Taniguchi, A. Vishwanath, and P. Kim, Nature (London) 583, 221 (2020).
- [20] G. W. Burg, J. Zhu, T. Taniguchi, K. Watanabe, A. H. MacDonald, and E. Tutuc, Phys. Rev. Lett. 123, 197702 (2019).

- [21] Y. Cao, D. Rodan-Legrain, O. Rubies-Bigorda, J. M. Park, K. Watanabe, T. Taniguchi, and P. Jarillo-Herrero, Nature (London) 583, 215 (2020).
- [22] C. Shen, Y. Chu, Q. Wu, N. Li, S. Wang, Y. Zhao, J. Tang, J. Liu, J. Tian, K. Watanabe, T. Taniguchi, R. Yang, Z. Y. Meng, D. Shi, O. V. Yazyev, and G. Zhang, Nat. Phys. 16, 520 (2020).
- [23] G. Chen, L. Jiang, S. Wu, B. Lyu, H. Li, B. L. Chittari, K. Watanabe, T. Taniguchi, Z. Shi, J. Jung, Y. Zhang, and F. Wang, Nat. Phys. 15, 237 (2019).
- [24] G. Chen, A. L. Sharpe, P. Gallagher, I. T. Rosen, E. J. Fox, L. Jiang, B. Lyu, H. Li, K. Watanabe, T. Taniguchi, J. Jung, Z. Shi, D. Goldhaber-Gordon, Y. Zhang, and F. Wang, Nature (London) 572, 215 (2019).
- [25] G. Chen, A. L. Sharpe, E. J. Fox, Y.-H. Zhang, S. Wang, L. Jiang, B. Lyu, H. Li, K. Watanabe, T. Taniguchi, Z. Shi, T. Senthil, D. Goldhaber-Gordon, Y. Zhang, and F. Wang, Nature (London) 579, 56 (2020).
- [26] S. Chen, M. He, Y.-H. Zhang, V. Hsieh, Z. Fei, K. Watan-abe, T. Taniguchi, D. H. Cobden, X. Xu, C. R. Dean, and M. Yankowitz, Nat. Phys. 17, 374 (2021).
- [27] K.-T. Tsai, X. Zhang, Z. Zhu, Y. Luo, S. Carr, M. Luskin, E. Kaxiras, and K. Wang, arXiv:1912.03375.
- [28] T. Kariyado and A. Vishwanath, Phys. Rev. Res. 1, 033076 (2019).
- [29] K. Hejazi, Z.-X. Luo, and L. Balents, Proc. Natl. Acad. Sci. USA 117, 10721 (2020).
- [30] O. Can, T. Tummuru, R. P. Day, I. Elfimov, A. Damascelli, and M. Franz, Nat. Phys. 17, 519 (2021).
- [31] P. A. Volkov, J. H. Wilson, and J. H. Pixley, arXiv:2012.07860.
- [32] J. May-Mann and T. L. Hughes, Phys. Rev. B 101, 245126 (2020).
- [33] J. Cano, S. Fang, J. Pixley, and J. H. Wilson, Phys. Rev. B 103, 155157 (2021).
- [34] T. Wang, N. F. Q. Yuan, and L. Fu, Phys. Rev. X 11, 021024 (2021).
- [35] A. González-Tudela and J. I. Cirac, Phys. Rev. A 100, 053604 (2019).
- [36] Y. Fu, E. J. König, J. H. Wilson, Y.-Z. Chou, and J. H. Pixley, npj Quantum Mater. 5, 71 (2020).
- [37] T. Salamon, A. Celi, R. W. Chhajlany, I. Frérot, M. Lewenstein, L. Tarruell, and D. Rakshit, Phys. Rev. Lett. 125, 030504 (2020).
- [38] X.-W. Luo and C. Zhang, Phys. Rev. Lett. 126, 103201 (2021).
- [39] R. Bistritzer and A. H. MacDonald, Proc. Natl. Acad. Sci. USA 108, 12233 (2011).

- [40] R. Bistritzer and A. H. MacDonald, Phys. Rev. B 84, 035440 (2011).
- [41] J. M. B. Lopes dos Santos, N. M. R. Peres, and A. H. Castro Neto, Phys. Rev. B 86, 155449 (2012).
- [42] S. Shallcross, S. Sharma, E. Kandelaki, and O. A. Pankratov, Phys. Rev. B 81, 165105 (2010).
- [43] L.-J. Yin, J.-B. Qiao, W.-J. Zuo, W.-T. Li, and L. He, Phys. Rev. B **92**, 081406(R) (2015).
- [44] P. W. Anderson, Science 235, 1196 (1987).
- [45] I. Affleck and J. B. Marston, Phys. Rev. B 37, 3774 (1988).
- [46] J. B. Marston and I. Affleck, Phys. Rev. B 39, 11538 (1989).
- [47] X.-G. Wen and P. A. Lee, Phys. Rev. Lett. 76, 503 (1996).
- [48] D. H. Kim and P. A. Lee, Ann. Phys. 272, 130 (1999).
- [49] P. A. Lee, N. Nagaosa, and X.-G. Wen, Rev. Mod. Phys. 78, 17 (2006).
- [50] W. Rantner and X.-G. Wen, Phys. Rev. Lett. 86, 3871 (2001).
- [51] X.-G. Wen, Phys. Rev. B 65, 165113 (2002).
- [52] W. Rantner and X.-G. Wen, Phys. Rev. B 66, 144501 (2002).
- [53] M. Hermele, T. Senthil, M. P. A. Fisher, P. A. Lee, N. Nagaosa, and X.-G. Wen, Phys. Rev. B 70, 214437 (2004).
- [54] M. Hermele, T. Senthil, and M. P. A. Fisher, Phys. Rev. B 72, 104404 (2005).
- [55] L. Balents, SciPost Phys. 7, 48 (2019).
- [56] C. Mora, N. Regnault, and B. A. Bernevig, Phys. Rev. Lett. 123, 026402 (2019).
- [57] Z.-D. Song, B. Lian, N. Regnault, and B. A. Bernevig, Phys. Rev. B 103, 205412 (2021).
- [58] As a side note, in the context of the algebraic spin liquid, the Dirac velocity anisotropy for the spinons, which is controlled by the deviation of t/Δ from 1, has been shown to be irrelevant in the renormalization group sense in the large- N_f limit [54,65,66]. Here, N_f refers to the number of flavor of spinons.
- [59] F. Guinea, M. I. Katsnelson, and M. A. H. Vozmediano, Phys. Rev. B 77, 075422 (2008).
- [60] T. O. Wehling, A. V. Balatsky, A. M. Tsvelik, M. I. Katsnelson, and A. I. Lichtenstein, Europhys. Lett. **84**, 17003 (2008).
- [61] I. Snyman, Phys. Rev. B 80, 054303 (2009).
- [62] L. Z. Tan, C.-H. Park, and S. G. Louie, Phys. Rev. B 81, 195426 (2010).
- [63] E. Tang and L. Fu, Nat. Phys. 10, 964 (2014).
- [64] M. O. Goerbig, arXiv:0909.1998.
- [65] O. Vafek, Z. Tešanović, and M. Franz, Phys. Rev. Lett. 89, 157003 (2002).
- [66] M. Franz, Z. Tešanović, and O. Vafek, Phys. Rev. B 66, 054535 (2002).